GEOPHYSICS, VOL. 64, NO. 1 (JANUARY-FEBRUARY 1999); P. 240–250, 7 FIGS., 5 TABLES.

Elastic finite-difference method for irregular grids

Ivo Opršal* and Jiří Zahradník*

ABSTRACT

Finite-difference (FD) modeling of complicated structures requires simple algorithms. This paper presents a new elastic FD method for spatially irregular grids that is simple and, at the same time, saves considerable memory and computing time. Features like faults, low-velocity layers, cavities, and/or nonplanar surfaces are treated on a fine grid, while the remaining parts of the model are, with equal accuracy, represented on a coarse grid. No interpolation is needed between the fine and coarse parts due to the rectangular grid cells. Relatively abrupt transitions between the small and large grid steps produce no numerical artifacts in the present method. Planar or nonplanar free surfaces, including underground cavities, are treated in a way similar to internal grid points but with consideration of the zero-valued elastic parameters and density outside the free surface (vacuum formalism). A theoretical proof that vacuum formalism fullfills the free-surface conditions is given. Numerical validation is performed through comparison with independent methods, comparing FD with explicitly prescribed boundary conditions and finite elements. Memory and computing time needed in the studied models was only about 10 to 40% of that employing regular square grids of equal accuracy. A practical example of a synthetic seismic section, showing clear signatures of a coal seam and cavity, is presented. The method can be extended to three dimensions.

INTRODUCTION

The finite difference (FD) method is a useful tool for seismic wave propagation modeling. Two approaches can be used at material discontinuities: (1) The equations of motion are combined with the traction-continuity conditions, or (2) only the equations of motion are solved, while the material parameters are treated as discontinuous functions. The latter is sometimes called the "heterogeneous approach." It dates back more than 30 years to Tikhonov and Samarskii (1961), Boore (1972), and Kelly et al. (1976), but recently it was theoretically justified (Zahradník and Priolo, 1995). The methods work with material parameters geometrically averaged (defined later) along the grid legs between any two neighboring grid points. The geometric averaging is essential for correct representation of the true position of the interface passing between the grid points (Figure 2 of Zahradník, 1995) and for keeping the interface free of a staircase deformation. Similar conclusions have been drawn by Nielsen (1994) and Graves (1996).

The "vacuum formalism" of Zahradník et al. (1993) approximates the free surface by the same formulas as the internal grid points while considering a part of its neighborhood as a vacuum. The surface points require the full-form FD method, whereas either the full-form or a simpler short-form method can be used at the internal grid points (Zahradník, 1995). Vacuum formalism is appealing for its simplicity compared to other FD methods employed for topography problems (e.g., Jastram and Tessmer, 1994; Hestholm and Ruud, 1994; Tessmer et al., 1992; Jih et al., 1988; Falk et al., 1995; Robertson, 1996). If, however, vacuum formalism is applied at the nonplanar free surface, the free surface gets a staircase form. This unfavorable property contrasts with the better behavior of methods with geometric averages at internal discontinuities, whose form is correctly followed between the grid lines without the staircase distortion. The free surface gets a staircase form because the geometric average along any leg whose part (whatever small part) is in vacuum becomes automatically zero valued. For 3-D methods with vacuum formalism, see Graves (1997), Ohminato and Chouet (1997), and Pitarka and Irikura (1996).

A compromise keeping the simplicity of vacuum formalism but improving its performance at nonplanar free surfaces is the employment of a spatially irregular grid. This allows the grid refinement at prominent topography features, and relatively coarse gridding (more quantitatively described below) at flat topography parts.

Although topography was our main motivation for the irregular grids, irregular gridding is highly advantageous also inside the medium, for at least two reasons: (1) When low-velocity regions occupy relatively small parts of the model, grid refined in

Manuscript received by the Editor February 3, 1997; revised manuscript received June 2, 1998.
*Charles University, Department of Geophysics, Faculty of Mathematics and Physics, V Holesovickach 2, 180 00 Praha 8, Czech Republic. E-mail: io@karel.troja.mff.cuni.cz; jz@karel.troja.mff.cuni.cz.

those regions can be used. Oversampling of large high-velocity areas, typical for fine regular grids, is avoided in that way. (2) Grid refinements in vicinities of material discontinuities partly compensate for the fact that the heterogeneous approach has a lower approximation order there (e.g., the second order inside a block transforms to the first order at a discontinuity or free surface).

Therefore, the objective of this paper is to develop a new FD method for spatially irregular grids and to apply it to both nonplanar topography and internal discontinuities. We start from the *PS*-2 method for regular grids (Zahradník, 1995), and study a simple case of so-called "rectangular irregular grids," which avoid any interpolation between the coarse and fine parts (Figure 1a).

For similar (rectangular) grids and the SH-waves case, see Moczo (1989). For more general irregular grids and SH-waves, see Moczo et al. (1996). This method, however, may have stability problems for the P-SV case (grids $h \times h$ neighboring with $2h \times 2h$; Moczo et al., 1997). For staggered irregular grids and P-SV waves, see Jastram and Tessmer (1994) and Falk et al. (1996). None of the cited authors reported testing of a more abrupt change of the grid step than 1:3. For grids with locally varying time steps, see Falk et al. (1995). For deforming the rectangular grid into a curved grid with the topmost grid line right on the curved surface, see Tessmer et al. (1992) and Hestholm and Ruud (1994). A promising combination of FD and finite elements for treating complex models has been suggested recently by Moczo et al. (1997).

DERIVATION OF IRREGULAR-GRID METHOD

Seismic waves in a 2-D perfectly elastic, isotropic, heterogeneous medium separate into P-SV and SH types. The P-SV waves are described by the equations of motion,

$$\frac{\partial}{\partial x}\left((\lambda+2\mu)\frac{\partial u}{\partial x}\right)+\frac{\partial}{\partial z}\left(\mu\frac{\partial u}{\partial z}\right)+\frac{\partial}{\partial x}\left(\lambda\frac{\partial w}{\partial z}\right)+\frac{\partial}{\partial z}\left(\mu\frac{\partial w}{\partial x}\right)=\rho\frac{\partial^2 u}{\partial t^2}, \tag{1}$$

$$\frac{\partial}{\partial x}\left(\mu\frac{\partial w}{\partial x}\right)+\frac{\partial}{\partial z}\left((\lambda+2\mu)\frac{\partial w}{\partial z}\right)+\frac{\partial}{\partial x}\left(\mu\frac{\partial u}{\partial z}\right)+\frac{\partial}{\partial z}\left(\lambda\frac{\partial u}{\partial x}\right)=\rho\frac{\partial^2 w}{\partial t^2}, \tag{2}$$

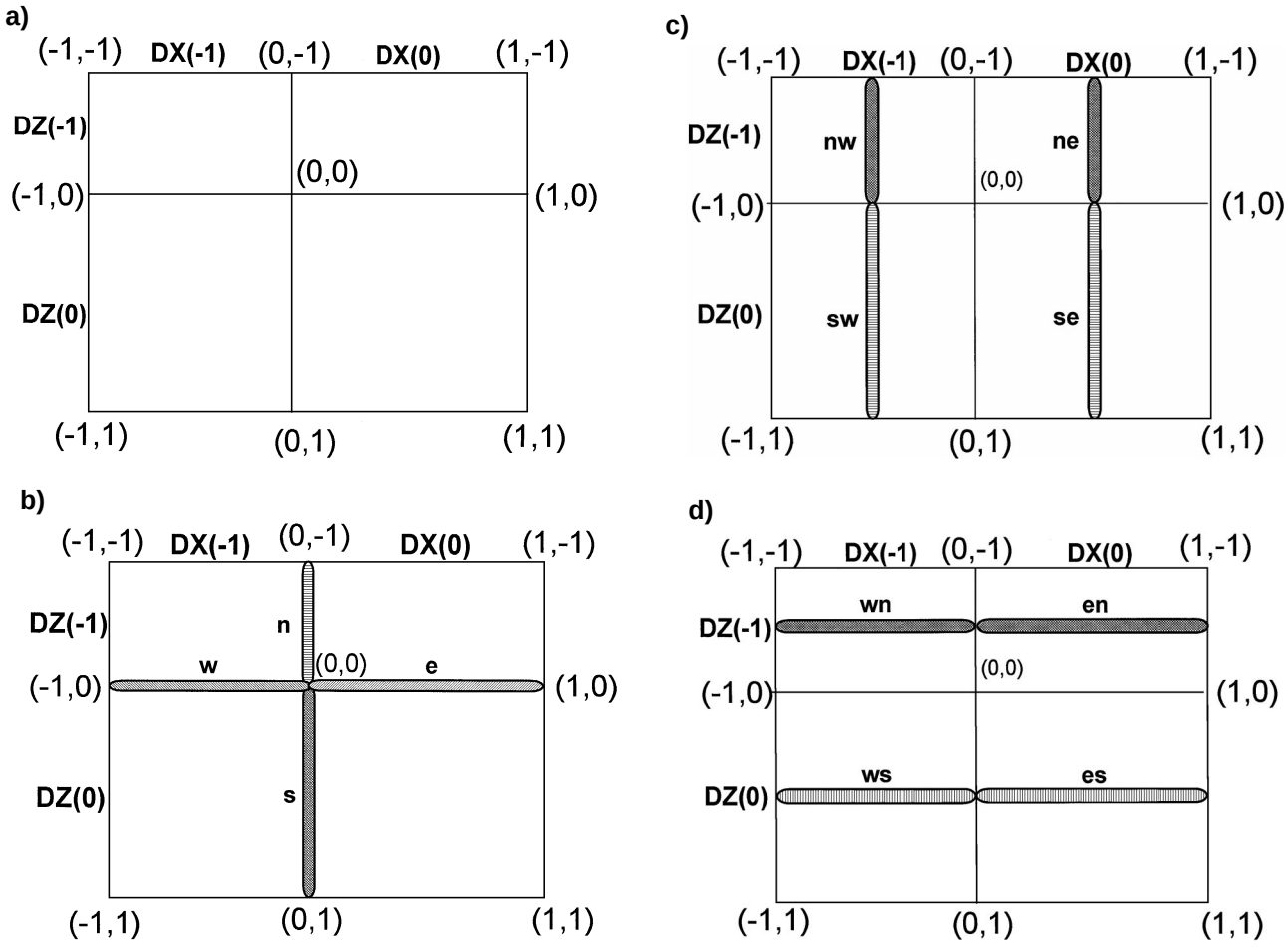

FIG. 1. The stencil for the FD approximations. (a) Denotation of the gridpoints and the gridsteps for an FD cell. (b) The vertical and horizontal parameters for the short-form approximation to $\partial(a\partial f/\partial z)/\partial x$, $\partial(a\partial f/\partial x)/\partial z$, and also for the approximation to $\partial(a\partial f/\partial z)/\partial z$ and $\partial(a\partial f/\partial x)/\partial x$. (c) The vertical parameters for the full-form approximation to $\partial(a\partial f/\partial x)/\partial z$. (d) The horizontal parameters for the full-form approximation to $\partial(a\partial f/\partial z)/\partial x$.

where u and w denote the horizontal and vertical displacement components, respectively. The parameters λ and μ are Lamé's elastic coefficients; ρ is the density.

Hereafter, we derive an FD approximation to two typical terms of equations (1) and (2): $\partial(a\partial f/\partial x)/\partial z$ and $\partial(a\partial f/\partial z)/\partial z$, called mixed and nonmixed derivatives, respectively. Here a is elastic parameter, and f either vertical or horizontal displacement component. The mixed and nonmixed derivatives are obtained in way analogous to that used in Zahradník (1995).

The mixed derivative is approximated in short and full forms. The short form is suitable for computation in all the grid points lying inside the medium, including also grid points at interfaces. Using the short form method at the free surface leads an extra body force, artificially created at the surface points, that violates the stress-free condition [equation (13) of Zahradník (1995)]. To satisfy the stress-free conditions, the full form must be used. It may be applied also at all internal points, but it employs more arithmetic operations than the short form.

To derive the mixed derivative approximation in short form, we take

$$\frac{\partial}{\partial z}\left(a\frac{\partial f}{\partial x}\right) = \frac{\partial}{\partial z}g, \tag{3}$$

where

$$\left.\frac{\partial}{\partial z}g\right|_{0,0} \approx 2\frac{g_{0,\frac{1}{2}} - g_{0,-\frac{1}{2}}}{(DZ(-1) + DZ(0))}. \tag{4}$$

Further, after applying integration in the z-direction and the mean value theorem, the g value at the point $(0, \frac{1}{2})$ is approximated by

$$g_{0,\frac{1}{2}} \approx \frac{a_s}{DZ(0)}\int_{(0,0)}^{(0,1)}\left.\frac{\partial f}{\partial x}\right|_{x=0} dz \approx \frac{a_s}{DZ(0)}\left.\frac{\partial f}{\partial x}\right|_{0,\frac{1}{2}} DZ(0)$$

$$\approx a_s\frac{f_{1,\frac{1}{2}} - f_{-1,\frac{1}{2}}}{DX(-1) + DX(0)}. \tag{5}$$

Here a_s represents the effective material parameter along the grid leg denoted as S in Figure 1b. That is why equation (5) is more sophisticated than a simple central difference. According to equation (5), the effective parameter a_s is defined as a geometric average of the actual parameter a along the corresponding gridleg; e.g.,

$$a_s = DZ(0)\Big/\int_{(0,0)}^{(0,1)}\frac{dz}{a(z)}. \tag{6}$$

In a special case of an interface coinciding with the grid leg, the effective parameter a_s is taken as an arithmetic average from the two neighboring media (Boore, 1972). Assuming further $f_{1,1/2}$ and $f_{-1,1/2}$ to be arithmetic averages of the neighboring values, then

$$g_{0,\frac{1}{2}} \approx \frac{a_s}{DX(-1) + DX(0)}\frac{1}{2}((f_{1,0} + f_{1,1}) - (f_{-1,0} + f_{-1,1})). \tag{7}$$

Treating $g_{0,-1/2}$ likewise leads to the short form approximation of the mixed derivative:

$$\frac{\partial}{\partial z}\left(a\frac{\partial f}{\partial x}\right) \approx \frac{1}{DZ(-1) + DZ(0)}\frac{1}{DX(-1) + DX(0)} \times [a_s(f_{1,0} + f_{1,1} - f_{-1,0} - f_{-1,1}) - a_n(f_{1,-1} + f_{1,0} - f_{-1,-1} - f_{-1,0})]. \tag{8}$$

Parameters a_n and a_s are effective parameters, as shown in Figure 1b. Using an analogous procedure with parameters a_e and a_w, we obtain the approximation for $\partial(a\partial f/\partial z)/\partial x$.

The mixed derivative in full form is derived similarly, but the initial approximation to $\partial g/\partial z$ is slightly different (see Figures 1c, 1d):

$$\frac{\partial}{\partial z}g \approx \frac{\left(g_{-\frac{1}{2},\frac{1}{2}} + g_{\frac{1}{2},\frac{1}{2}}\right) - \left(g_{-\frac{1}{2},-\frac{1}{2}} + g_{\frac{1}{2},-\frac{1}{2}}\right)}{(DZ(-1) + DZ(0))}. \tag{9}$$

After applying the mean-value theorem, the g-value in point $(\frac{1}{2}, \frac{1}{2})$ is

$$g_{\frac{1}{2},\frac{1}{2}} \approx a_{se}\left.\frac{\partial f}{\partial x}\right|_{\left(\frac{1}{2},\frac{1}{2}\right)} \approx \frac{a_{se}}{DX(0)}\left(f_{1,\frac{1}{2}} - f_{0,\frac{1}{2}}\right);$$

thus,

$$g_{\frac{1}{2},\frac{1}{2}} \approx \frac{a_{se}}{2DX(0)}(f_{1,0} + f_{1,1} - f_{0,0} - f_{0,1}). \tag{10}$$

The complete stencil, made of four parts constructed similarly, is

$$\frac{\partial}{\partial z}\left(a\frac{\partial f}{\partial x}\right) = \frac{\partial}{\partial z}g \approx \frac{\frac{1}{2}}{DZ(-1) + DZ(0)}\left[a_{se}\cdot\frac{1}{DX(0)} \times (f_{1,0} + f_{1,1} - f_{0,0} - f_{0,1}) + a_{sw}\frac{1}{DX(-1)}(f_{0,0} + f_{0,1} - f_{-1,0} - f_{-1,1}) - a_{ne}\frac{1}{DX(0)}(f_{1,-1} + f_{1,0} - f_{0,-1} - f_{0,0}) - a_{nw}\frac{1}{DX(-1)}(f_{0,-1} + f_{0,0} - f_{-1,-1} - f_{-1,0})\right]. \tag{11}$$

Parameters a_{se}, a_{sw}, a_{ne}, and a_{nw} are effective parameters belonging to the particular legs of the finite difference stencil (see Figure 1c). The derivative $\partial(a\partial f/\partial z)/\partial x$ is quite analogous with parameters a_{es}, a_{ws}, a_{en}, and a_{wn}.

For the nonmixed derivatives $\partial(a\partial f/\partial z)/\partial z$ and $\partial(a\partial f/\partial x)/\partial x$, there is no need to distinguish the full and short forms. The only approximation is similar to the mixed derivative short form:

$$\frac{\partial}{\partial z}\left(a\frac{\partial f}{\partial z}\right) \approx \frac{g_{0,\frac{1}{2}} - g_{0,-\frac{1}{2}}}{\frac{1}{2}(DZ(-1) + DZ(0))} = 2\frac{1}{DZ(-1) + DZ(0)}\left(a_s\frac{f_{0,1} - f_{0,0}}{DZ(0)} - a_n\frac{f_{0,0} - f_{0,-1}}{DZ(-1)}\right), \tag{12}$$

with parameters a_n and a_s, shown in Figure 1b.

Let us insert the space derivatives into equations (1) and (2), and denote their left sides as L_u and L_w, respectively. Then, after applying a standard time differentiation (with a time step Δt), we get the final second-order method:

$$U_{0,0}^{M+1} = \frac{(\Delta t)^2}{\rho_{0,0}} L_u^M(u, w) + 2U_{0,0}^M - U_{0,0}^{M-1}, \quad (13)$$

$$W_{0,0}^{M+1} = \frac{(\Delta t)^2}{\rho_{0,0}} L_w^M(u, w) + 2W_{0,0}^M - W_{0,0}^{M-1}. \quad (14)$$

For a complete description of L_u and L_w, see the Appendix. Special treatment (to satisfy the traction-free condition) has to be given to ρ. Let $\tilde{\rho}$ be the density below the surface. Then, for the grid points at the planar (horizontal or vertical) parts of the surface, $\rho_{0,0} = \tilde{\rho}/2$, whereas for the outer and inner corners (see Figure 2a), $\rho_{0,0} = \frac{1}{4}\tilde{\rho}$ and $\rho_{0,0} = \frac{3}{4}\tilde{\rho}$, respectively. The legs coinciding with the free surface must have their effective parameters halved with respect to values inside. These rules follow from the requirement that the FD method automatically approximates the free-surface condition, as detailed below. The FD method has been derived for the 2-D case, but its generalization to three dimensions is straightforward.

CONSISTENCY WITH FREE SURFACE CONDITIONS

We investigate the boundary behaviour of our method for typical surface configurations by inserting 2-D Taylor's expansion of the u and w components into the FD equations (13) and (14). In this case, for simplicity, we assume a regular grid with grid steps $\Delta x = \Delta z = h$, and a homogeneous medium with λ and μ being the elastic parameters. The free-surface specifications are in Figure 2a. As regards the flat horizontal and vertical parts, when aligned to grid lines, the Taylor's expansion of the method is then equivalent to the first order ($O(h)$) approximation to the standard free surface condition (see, e.g., Zahradník et al., 1993). A different situation appears at the corners (i.e., the elements of the staircase free surface). After a simple formal procedure with equations (13) and (14), we get the following equations for the outer corner grid point in Figure 2a:

$$-(\lambda + 2\mu)U_x + \mu U_z - \lambda W_z + \mu W_x = 0 + O(h) + O((\Delta t)^2), \quad (15)$$

$$-\mu W_x + (\lambda + 2\mu)W_z - \mu U_z + \lambda U_x = 0 + O(h) + O((\Delta t)^2). \quad (16)$$

The same approximations (15) and (16) hold also for the inner corner (Figure 2a). When compared to the general form of the stress-free condition [equation (9) of Zahradník et al., 1993], equations (15) and (16) say that our heterogeneous approach applied to the corner is equal to the linear combination of the free-surface conditions for the horizontal and vertical free surface, with an equal weight. In other words, equations (15) and (16) are equivalent to the condition at a flat free surface inclined by 45°.

STABILITY AND ACCURACY

For the second-order explicit method on a regular square grid, there is a theoretically derived stability condition relating the spatial gridstep h and the timestep Δt (Virieux, 1986): $\Delta t \leq h/\sqrt{2}\alpha_{max}$, where α_{max} is the highest P-wave velocity in

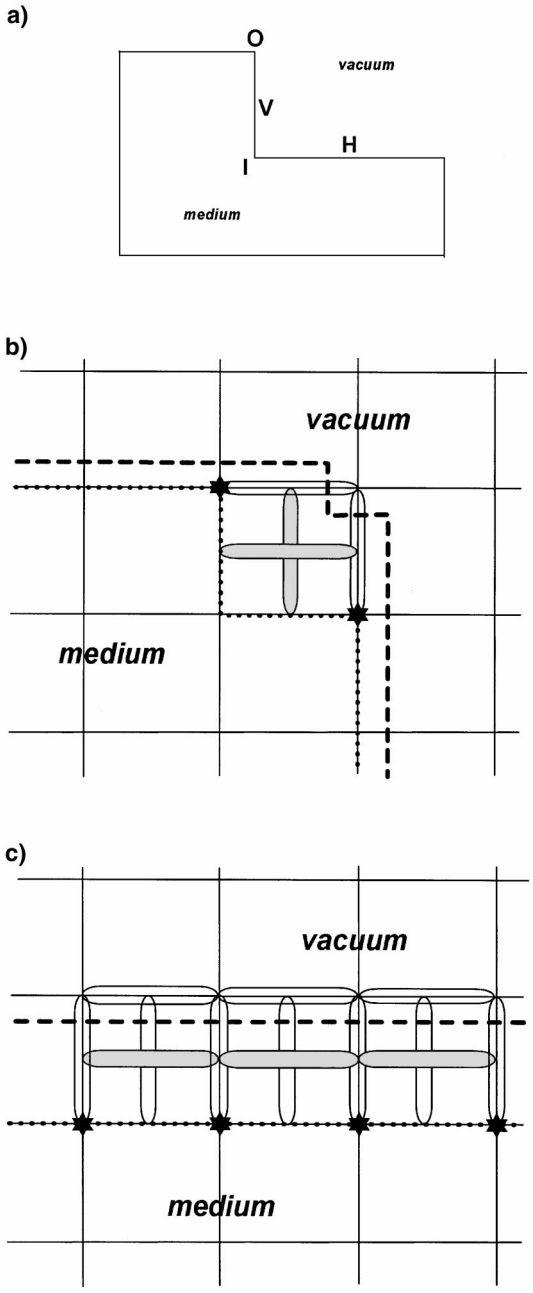

FIG. 2. (a) A schematic free-surface model with corners: H = horizontal part, V = vertical part, O = outer corner, I = inner corner. (b) and (c) Situations causing instability when computing in grid points denoted by stars. The dashed line represents a prescribed surface, the effective parameters are distinguished as zero valued (white ovals) and nonzero (gray ovals). The dotted line represents the free-surface modification necessary to stabilize the *PSi*-2 method: the method is stabilized by avoiding combinations of the zero and nonzero parameters within a grid cell.

the medium. For our heterogeneous formulation on an irregular grid, applied to nonplanar surfaces and internal discontinuities, we use a stability condition $\Delta t \le h_{min}/c\alpha_{max}$, where h_{min} denotes the minimal gridstep appearing in the irregular grid, Δt is the time step (constant for the entire computation), and $c = 1.6$, empirically found in our numerical experiments.

To keep numerical dispersion at a reasonably low level (Alford et al., 1974), we determine the largest possible grid steps $\widetilde{\Delta x}_{max} = \widetilde{\Delta z}_{max} = \tilde{h}$ in every particular region of the model by

$$\tilde{h} = \frac{\tilde{\beta}}{10\, f^*_{max}}, \qquad (17)$$

where f^*_{max} is the frequency at which the time function spectrum falls below 1% of its maximum value and $\tilde{\beta}$ is the S-wave velocity in the area.

Although satisfying the mentioned conditions, a significant instability, which cannot be stabilized by refining the grid step or time step, sometimes emerges in practical applications. However, such situations can be stabilized by weak artificial distortions of the surface shape. To explain this, let us recall that the effective parameters get zero values if the original free surface line intersects the grid leg between two neighboring grid points. At the same time, it may happen that the other legs of the same grid cell have nonzero effective parameters. Such combinations of the zero and nonzero parameters yield instabilities. Two examples are shown in Figures 2b and 2c. To stabilize the solution, we have to adjust the effective parameters along gray legs to zero. This is equivalent to shifting the surface into the dotted line position. To avoid these problems, the computer code should automatically check all grid points in the vicinity of the free surface, and perturb the model surface according to a simple rule: no mixing of zero and nonzero effective parameters within a grid cell. Finally, before the FD computation, the entire surface is artificially aligned to vertical and/or horizontal grid lines, which produces a stable staircase approximation to the originally prescribed surface form.

EXAMPLE 1: TWO QUARTER SPACES

A two quarter-space model (see Figure 3a and Table 1) is first investigated on a regular grid: $\Delta x = \Delta z = 4.0$ m. Tapers of 40 points (Cerjan et al., 1985), and Stacey's (1988) boundary conditions are applied along the bottom and the right edges. Symmetry in $w[w(-x, z) = w(x, z)]$ and antisymmetry in $u[u(-x, z) = -u(x, z)]$ are applied along the left edge along the line $[(0, 0), (0, 960)]$. The line source placed near the surface (Figure 3a) is realized by a vertical body force whose time history is

$$f(t) = -\exp(b)\, f_{max}[\, f_{max}(t - t_0)\cos c + \pi \sin c], \qquad (18)$$

where $b = -\frac{1}{2} f^2_{max}(t - t_0)^2$, $c = \pi f_{max}(t - t_0)$, with $t_0 = 0.136$ s and the maximum frequency $f_{max} = 22$ Hz. Our results are compared with the spectral-element method (SPEM) of Priolo et al. (1994) in Figures 3b, 3c, and 3d and in Table 3.

Next, as shown in Table 2, the same two quarter-space model has an irregular grid (see Figure 4a). It is realized in the following way: the first 10 grid steps between horizontal lines $\ell = 1$, and $\ell = 11$ are of $\Delta z = 0.8$ m. Then, between grid lines $\ell = 11$ and $\ell = L_{max}$, the grid steps are of $\Delta z = 4.0$ m. Similarly for the vertical lines (Figure 4a), the grid steps are $\Delta x = 4.0$ m between grid lines $k = 1$ and $k = 252$, then $\Delta x = 0.8$ m between grid lines $k = 252$ and $k = 267$, and finally $\Delta x = 4.0$ m between grid lines $k = 267$ and $k = K_{max}$. The interface is lying exactly in the middle between vertical lines $k = 259$ and $k = 260$.

The results calculated by *PSi-2* are compared with the SPEM method in Figures 4b–d. The agreement is better than in the case of the regular grid. The most significant improvement is marked by arrows. Table 3 shows the comparison of the true maxima values n_R. Compared to a model with fine regular grid (not presented here), we save up to 90% of computing time and about 95% of memory in this model with an irregular grid, whereas the solutions with a fine regular grid and with an irregular grid do not differ within the thickness of the line.

Table 1. Parameters of numerical example 1 for the model with a regular grid.

Parameter*	Value
α_I	2000
β_I	1155
ρ_I	1000
α_{II}	3000
β_{II}	1732
ρ_{II}	2000
f^*_{max}	22
Δt	0.0005
Δx	4.0
Δz	4.0
N_t	4000
K	512
L	242

*α_I, β_I = P-, S-wave velocities (m/s) in block I; ρ_I = density (kg/m^3) in block I; α_{II}, β_{II} = analogs for block II; f^*_{max} = the frequency (Hz) at which the absolute value of the spectrum is 1% of the maximum spectral value; Δt = time step (s); $\Delta x, \Delta z$ = grid steps (m); N_t = number of time steps; K, L = number of vertical and horizontal lines in the model.

Table 2. Parameters of numerical example 1 for the model with an irregular grid.

Parameter*	Value
α_I	2000
β_I	1155
ρ_I	1000
α_{II}	3000
β_{II}	1732
ρ_{II}	2000
f^*_{max}	22
Δt	0.0001
Δx_{min}	0.8
Δz_{min}	0.8
Δx_{max}	4.0
Δz_{max}	4.0
N_t	4000
K	512
L	350

*α_I, β_I = P-, S-wave velocities (m/s) in block I; ρ_I = density (kg/m^3) in block I; α_{II}, β_{II} = analogs for block II; f^*_{max} = the frequency (Hz) at which the absolute value of the spectrum is 1% of the maximum spectral value; Δt = time step (s); $\Delta x_{min}, \Delta z_{min}, \Delta x_{min}, \Delta z_{min}$ = the minimum and the maximum grid steps (m) appearing in the model; N_t = number of time steps; K, L = number of vertical and horizontal lines in the model.

Another important result from these experiments (and equally well from the other experiments we have done) is that the *PSi*-2 methods allows an abrupt change in the grid step size without numerical artifacts. The abrupt change means that two neighboring grid steps may differ by a factor of 20 without any significant change in the solution. At the same time, the coarser part of the grid must be still fine enough with respect to the shortest wavelength (e.g., a standard 10 grid points per wavelength).

EXAMPLE 2: STEPLIKE SURFACE OF HOMOGENEOUS HALF-SPACE

In this model, we investigate the down-step surface of a homogeneous half-space with an explosive line source, *S*. The

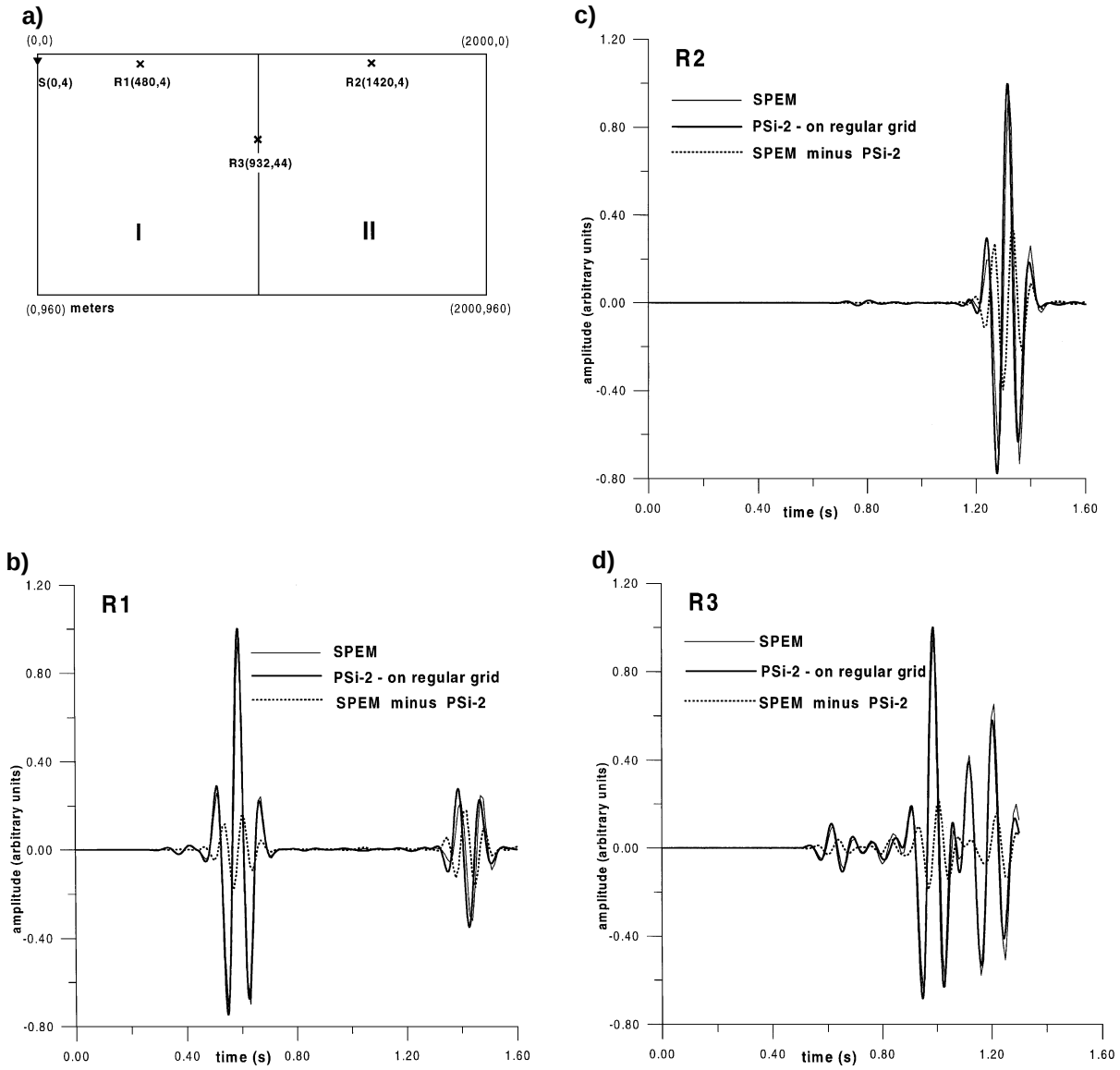

FIG. 3. Two quarter-spaces on a regular grid. (a) The model (coordinates in meters): S = source, R = receivers. For details see Table 1. (b–d) Seismograms (vertical component) at receivers R1, R2, and R3, calculated by the *PSi*-2 method on a regular grid. For comparison, the spectral-element method (SPEM) solution of Priolo et al. (1994) is also presented (thin line). Signal at R3 is shorter to avoid the reflections from the model edges. The difference between the SPEM and *PSi*-2 solutions is shown by the dotted line.

Table 3. Relative true maxima values for example 1 models with regular and irregular grids.

Method	n^*_{R1u}	n_{R2u}	n_{R2u}	n_{R1w}	n_{R2w}	n_{R2w}
PSi-2 regular grid	0.385	0.174	0.0565	1.00	0.373	0.0676
PSi-2 irregular grid	0.337	0.170	0.0620	1.00	0.373	0.0662
SPEM	0.380	0.171	0.0612	1.00	0.373	0.0592

*n_{R1u} is the true maximum values for u component in receiver R1, and analogously for the other receivers and component w.

receivers $R1$, $R2$, and $R3$ are placed as shown in Figure 5a. First, the grid of the model is regular, with grid step $\Delta x = \Delta z = 1.0$ m. The time function for the explosive source is a finite-duration approximation to Dirac's δ-function (Aboudi, 1971), with duration $T = 0.003$ s. There are no artificial reflections in the model because the arrival time of possible reflections from the boundaries is greater than that of the time window. The parameters of the model are in Table 4.

The results were compared with Hong and Bond (1986) in Figure 5b. Their method in contrast to our heterogeneous scheme is a homogeneous FD scheme, i.e, the formulas for internal grid points differ from those for the free surface. Moreover, for the corner grid points special formulas are used (see Table 1 in their paper).

Our model was exactly the same as that of Hong and Bond (hereafter called "original data"), including the employed grid steps. Therefore, the numerical dispersion due to the coarse grid (Alford et al., 1974) appears in both results. As seen in Figure 5b and Table 5, a close agreement of our solution with that of Hong and Bond exists.

Second, we also computed this model on an irregular grid, where the coarse part (with enough dispersion) was the same

Table 4. Parameters of numerical example 2, with variables as in Table 3.

Parameter*	Value
α_I	5000
β_I	$5000/\sqrt{3}$
ρ_I	1000
f^*_{max}	1000
Δt	0.0001
Δx	1.0
Δz	1.0
N_t	350
K	320
L	100

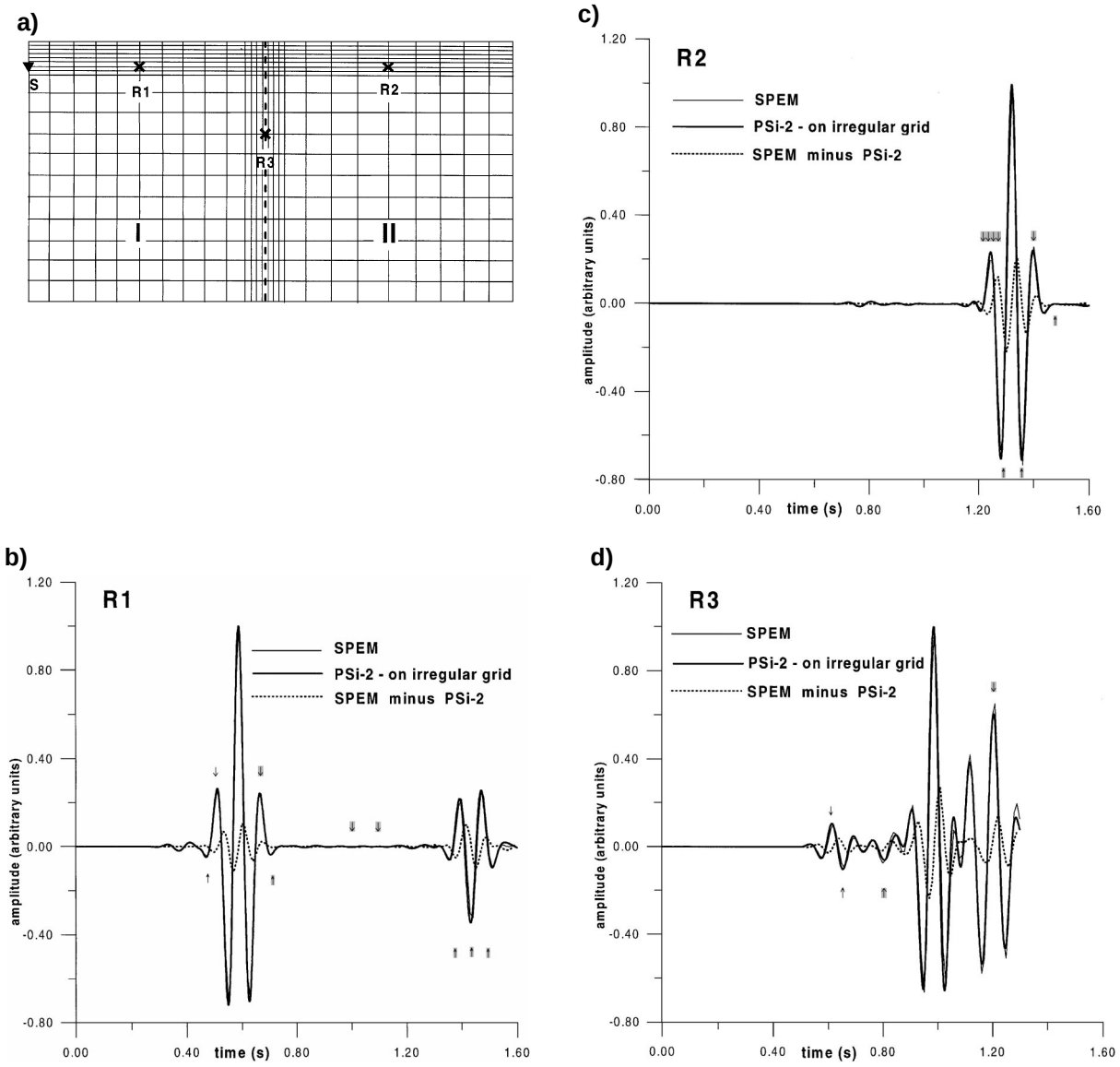

FIG. 4. Two quarter-spaces on an irregular grid. (a) Denser gridding along the horizontal free surface and vertical interface (dashed line). (b–d) Seismograms (vertical component) at receivers R1, R2, and R3, compared to the SPEM solution of Priolo et al. (1994). Signal at R3 is shorter to avoid the reflections from the model edges. The difference between the SPEM and *PSi*-2 solutions is shown by the dotted line. The significant improvements compared to Figures 3b–d are indicated by arrows.

as before, but the grid was refined just within 4 grid steps along the free surface (Figure 5c-2). It was refined abruptly with a ratio 1/4 between two neighboring grid steps. Third, we computed the same model on a regular fine grid (Figure 5c-3) with grid step 4 times smaller than in the Hong and Bond model. Finally, we computed the model on another irregular grid, now with coarse grid step 4 times smaller than in the Hong and Bond model, furthermore refined 3 times along the free surface. This time, the grid step change was smooth, as detailed in Figure 5c-4. But the abrupt change, not presented, also gave results with negligible differences. These results (Figure 5d) show that if the coarser part of the grid does not fulfill the condition for low dispersion, then refinement along the surface yields numerical artifacts (dashed line), e.g., spurious oscillations between 0.010 and 0.020 s. When the regular grid fulfills the condition, we obtain a better, nondispersive solution (solid line), which can be further improved by a smooth or abrupt refinement of the grid along the free surface and interfaces.

Table 5. True maxima values for example 2, a regular coarse grid.

Method	n^*_{R1u}	n_{R2u}	n_{R2u}	n_{R1w}	n_{R2w}	n_{R2w}
PSi-2	1.00	0.49	0.42	0.53	0.16	0.13
Original data**	1.00	0.46	0.41	0.47	0.14	0.13

*n_{R1u} is the true maximum values for u component in receiver R1, and analogously for the other receivers and component w.
**Hong and Bond (1986).

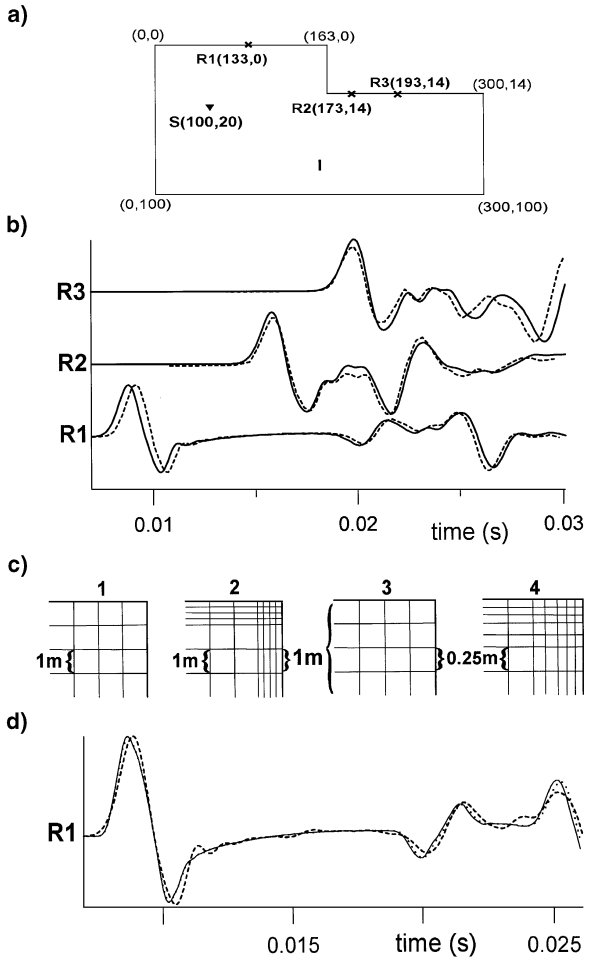

FIG. 5. Steplike surface of homogeneous half-space. (a) The model (coordinates in meters). (b) Seismograms for vertical component at receivers R1, R2, and R3 (full line) computed on a regular grid as shown in (c1), compared to the original Hong and Bond (1986) solution (dashed line). (c) Irregular-grid details and the way of its refinement along a part of the steplike surface: 1—original Hong and Bond (1986) meshing used in panel (b), 2—abrupt change in the grid step after refinement of grid 1, 3—well-meshed regular grid, 4—smooth change after refinement of grid 3. (d) Comparison of the solutions: dashed line = 2, dotted line = 3, and full line = 4. Notice the scale change when going from (a) and (b) to (c) and (d).

EXAMPLE 3: UNDERGROUND CAVITY AND COAL SEAM

An important practical problem in coal exploration is to detect heterogeneities in the coal overburden, such as boulders or cavities. We model a seismic section containing a single horizontal seam and cavity (Figure 6). The wavefield is excited by a line array of vertical forces along the free surface. A transient response due to Gabor's wavelet with a predominant frequency of 75 Hz is shown in Figure 7. The modeling is sufficiently accurate (10 grid points per wavelength in coal) up to 75 Hz. A significant irregularity of the employed grid, allowing correct

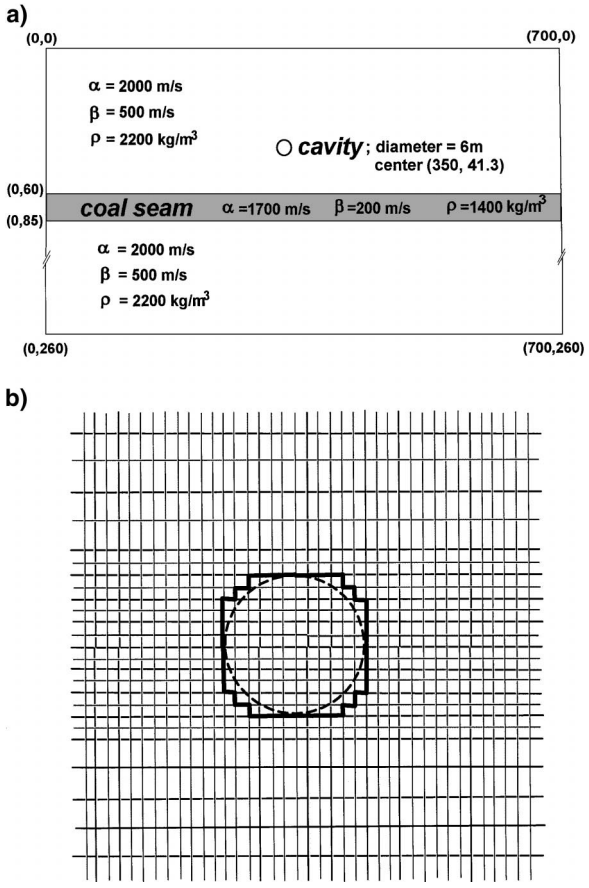

FIG. 6. Underground cavity and coal seam. (a) The model parameters (edge coordinates expressed in meters). (b) The refinement of the grid in vertical grid steps around the underground cavity. The true cavity (dashed circle) transforms into a staircase (thick line) shape.

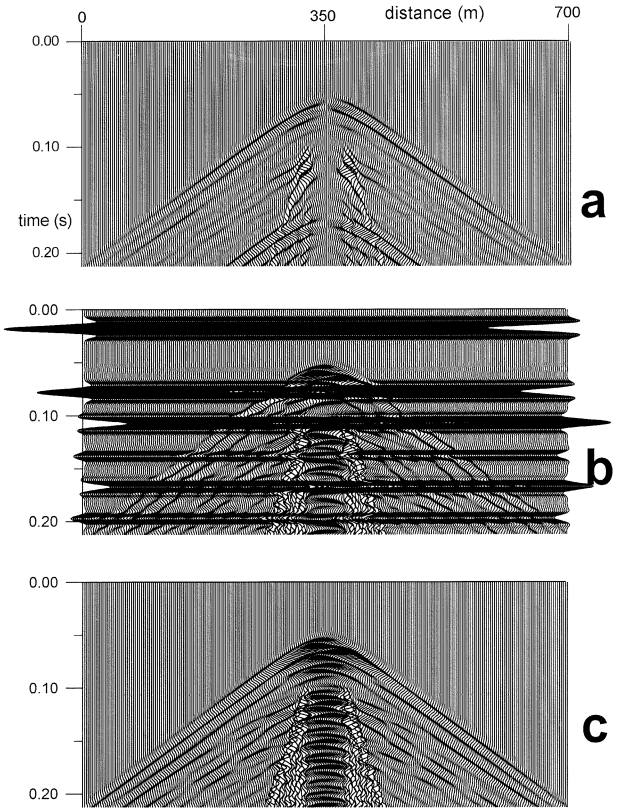

FIG. 7. Underground cavity and coal seam. (a) Horizontal and (b) vertical components of displacement. (c) Vertical component with the 1-D solution (without the cavity) subtracted. Receivers are located on the top flat free surface.

representation of the structural details, is used; at the same time, there is coarser grid in a major part of the model. As a result, both the seam and cavity have been clearly imaged with 60% computing time saved compared to the same model computed on a regular grid of the same accuracy (i.e., with negligible difference between the synthetics). These models were also computed without the cavity to obtain 1-D solutions that were subtracted from the complete solutions (Figures 7a, c). The same method also has been successfully used for elastic modeling of cavities filled with water.

CONCLUSION

The *PSi*-2 method represents a generalization of the regular-grid *PS*-2 method into irregular (rectangular) grids. The *PSi*-2 method on an irregular grid can provide results of the same accuracy as the *PS*-2 method on a fine regular grid, but with a considerably saving in memory and computer time. The *PSi*-2 method allows, without spurious numerical effects, changes of the grid step size between the dense and coarse parts of the grid (e.g., 1 : 20) that are more abrupt than the changes so far reported in the literature. Such abrupt changes of the grid step size are possible provided the coarse parts are guided at least by a standard 10 grid points per wavelength. The method allows the nonplanar topography treatment by vacuum formalism. Although vacuum formalism approximates the free surface by a staircase boundary (in contrast to keeping the true form of the internal boundaries), accuracy can be improved by grid refinement close to the nonplanar parts of the surface. In general, the FD program package based on heterogeneous methods with geometrically averaged material parameters, vacuum formalism, and irregular grids provides an efficient tool for a wide class of 2-D structures. At the same time, the employed methods are rather simple, so as to allow very easy data input, and do not need any program modifications when passing from one model to the other.

ACKNOWLEDGMENTS

The authors thank Dr. P. Moczo for many useful comments. This research was financially supported by Czech Republic grant GAČR 205/1743, Charles University grant No. 5/97, the NATO SfS GR-COAL grant, and the EU Inco-Copernicus grants COME and ISMOD.

REFERENCES

Aboudi, J., 1971, Numerical simulation of seismic sources: Geophysics, **36**, 810–821.
Alford, R. M., Boore, M. D., and Kelly, K. R., 1974, Accuracy of finite-difference modeling of the acoustic wave equation: Geophysics, **39**, 834–842.
Boore, D. M., 1972, Finite-difference methods for seismic waves, *in* Bolt, B. A., Ed., Methods in computational physics: Academic Press, **11**, 1–37.
Cerjan, C., Kosloff, R., and Reshef, M., 1985, A nonreflecting boundary condition for discrete acoustic and elastic wave equations: Geophysics, **50**, 705–708.
Falk, J., Tessmer, E., and Gajevski, D., 1995, Seismic modelling by the finite-difference method with locally varying timesteps: Presented at the 57th EAEG meeting, talk D013.
———1996, Tube wave modelling by the finite-differences method with varying grid spacing: Pageoph, **148**, 77–93.
Graves, R. W., 1996, Simulating seismic wave propagation in 3-D elastic media using staggered-grid finite differences: Bull. Seism. Soc. Am., **86**, 1091–1106.
Hestholm, S. O., and Ruud, B. O., 1994, 2-D Finite-difference elastic wave modeling including surface topography: Geophys. Prosp. **42**, 371–390.
Hong, M., and Bond, L. J., 1986, Application of the finite difference method in seismic source and wave diffraction simulation: Geophys. J. Roy. Astr. Soc., **87**, 731–752.
Jastram, C., and Tessmer, E., 1994, Elastic modelling on a grid with vertically varying spacing: Geophys. Prosp. **42**, 357–370.
Jih, R. S., McLaughlin, K. L., and Der, Z. A., 1988, Free-boundary conditions of arbitrary polygonal topography in a two-dimensional explicit elastic finite-difference scheme: Geophysics, **53**, 1045–1055.
Kelly, K. R., Ward, R. W., Treitel, S., and Alford, R. M., 1976, Synthetic seismograms: A finite-difference approach: Geophysics, **41**, 2–27.
Moczo, P., 1989, Finite-difference technique for *SH*-waves in 2-D media using irregular grids—Application to the seismic response problem: Geophys. J. Internat., **99**, 321–329.
Moczo, P., Bystrický, E., Kristek, J., Carcione, J., and Bouchon, M., 1997, Hybrid modelling of *P*-*SV* seismic motion at inhomogeneous viscoelastic topographic structures: Bull. Seism. Soc. Am., **87**, 1305–1323.
Moczo, P., Labák, P., Kristek, J., and Hron, F., 1996, Amplification and differential motion due to an antiplane 2-D resonance in the sediment valleys embedded in a layer over the half-space: Bull. Seism. Soc. Am., **86**, 1434–1446.
Nielsen, P., 1994, Numerical modelling of seismic waves: On the elimination of grid artifacts: Norsk Hydro Research Center research report.
Ohminato, T., and Chouet, B. A., 1997, A free-surface boundary condition for including 3-D topography in the finite difference method: Bull. Seism. Soc. Am., **87**, 494–515.
Pitarka, A., Irikura, K., 1996, Modeling 3-D surface topography by finite difference method: Kobe-JMA station site, Japan, case study: Geophysics, **23**, 2729–2732.
Priolo, E., Carcione, J., and Seriani, G., 1994, Numerical simulation of interface waves by high-order spectral modeling techniques: J. Accoust. Soc. Am., **95**, 681–693.
Robertson, J. O. A., 1996, A numerical free-surface condition for elastic/viscoelastic finite-difference modeling in the presence of

topography: Geophysics, **61**, 1921–1934.
Stacey, R., 1988, Improved transparent boundary formulation for the elastic-wave equation: Bull. Seism. Soc. Am., **78**, 2089–2097.
Tessmer, E., Kosloff, D., and Behle, A., 1992, Elastic wave propagation simulation in the presence of surface topography: Geophys. J. Internat., **108**, 621–632.
Tikhonov, A. N., and Samarskii, A. A., 1961, Homogeneous difference schemes: Z. Vycisl. Mat. i Mat. Fiz., **1**, 5–63.
Virieux, J., 1986, *P-SV* wave propagation in heterogeneous media: Velocity-stress finite difference method: Geophysics, **51**, 889–901.
Zahradník, J., 1995, Simple elastic finite-difference scheme: Bull. Seism. Soc. Am., **85**, 1879–1887.
Zahradník, J., Moczo, P., and Hron, F., 1993, Testing four elastic finite-difference schemes for behaviour at discontinuities: Bull. Seism. Soc. Am., **83**, 107–129.
Zahradník, J., and Priolo, E., 1995, Heterogeneous formulations of elastodynamic equations and finite-difference schemes: Geophys. J. Internat., **120**, 663–676.

APPENDIX

COMPLETE FORMULAS OF PSi-2 METHOD

Let us denote $L_u(u, w)$, and $L_w(u, w)$ the FD approximation to the left-hand side of equations (1) and (2), respectively. Then, the short forms are

$$
\begin{aligned}
L_u(u,w) &= 2\frac{1}{DX(-1)+DX(0)}\left((\lambda_e+2\mu_e)\frac{u_{1,0}-u_{0,0}}{DX(0)}\right.\\
&\left.-(\lambda_w+2\mu_w)\frac{u_{0,0}-u_{-1,0}}{DX(-1)}\right)+2\frac{1}{DZ(-1)+DZ(0)}\\
&\times\left(\mu_s\frac{u_{0,1}-u_{0,0}}{DZ(0)}-\mu_n\frac{u_{0,0}-u_{0,-1}}{DZ(-1)}\right)\\
&+\frac{1}{DZ(-1)+DZ(0)}\frac{1}{DX(-1)+DX(0)}\\
&\times[\lambda_e(w_{0,1}+w_{1,1}-w_{0,-1}-w_{1,-1})\\
&-\lambda_w(w_{-1,1}+w_{0,1}-w_{-1,-1}-w_{0,-1})]\\
&+\frac{1}{DZ(-1)+DZ(0)}\frac{1}{DX(-1)+DX(0)}\\
&\times[\mu_s(w_{1,0}+w_{1,1}-w_{-1,0}-w_{-1,1})\\
&-\mu_n(w_{1,-1}+w_{1,0}-w_{-1,-1}-w_{-1,0})], \qquad \text{(A-1)}
\end{aligned}
$$

and

$$
\begin{aligned}
L_w(u,w) &= 2\frac{1}{DX(-1)+DX(0)}\left(\mu_e\frac{w_{1,0}-w_{0,0}}{DX(0)}\right.\\
&\left.-\mu_w\frac{w_{0,0}-w_{-1,0}}{DX(-1)}\right)+2\frac{1}{DZ(-1)+DZ(0)}\\
&\times\left((\lambda_s+2\mu_s)\frac{w_{0,1}-w_{0,0}}{DZ(0)}-(\lambda_n+2\mu_n)\frac{w_{0,0}-w_{0,-1}}{DZ(-1)}\right)\\
&+\frac{1}{DZ(-1)+DZ(0)}\frac{1}{DX(-1)+DX(0)}\\
&\times[\mu_e(u_{0,1}+u_{1,1}-u_{0,-1}-u_{1,-1})\\
&-\mu_w(u_{-1,1}+u_{0,1}-u_{-1,-1}-u_{0,-1})]\\
&+\frac{1}{DZ(-1)+DZ(0)}\frac{1}{DX(-1)+DX(0)}\\
&\times[\lambda_s(u_{1,0}+u_{1,1}-u_{-1,0}-u_{-1,1})\\
&-\lambda_n(u_{1,-1}+u_{1,0}-u_{-1,-1}-u_{-1,0})]. \qquad \text{(A-2)}
\end{aligned}
$$

The full forms are

$$
\begin{aligned}
L_u(u,w) &= 2\frac{1}{DX(-1)+DX(0)}\\
&\times\left((\lambda_e+2\mu_e)\frac{u_{1,0}-u_{0,0}}{DX(0)}-(\lambda_w+2\mu_w)\frac{u_{0,0}-u_{-1,0}}{DX(-1)}\right)\\
&+2\frac{1}{DZ(-1)+DZ(0)}\left(\mu_s\frac{u_{0,1}-u_{0,0}}{DZ(0)}-\mu_n\frac{u_{0,0}-u_{0,-1}}{DZ(-1)}\right)\\
&+\frac{\frac{1}{2}}{DX(-1)+DX(0)}\left[\lambda_{es}\frac{1}{DZ(0)}(w_{0,1}+w_{1,1}\right.\\
&-w_{0,0}-w_{1,0})+\lambda_{en}\frac{1}{DZ(-1)}(w_{0,0}+w_{1,0}\\
&-w_{0,-1}-w_{1,-1})-\lambda_{ws}\frac{1}{DZ(0)}(w_{-1,1}+w_{0,1}\\
&-w_{-1,0}-w_{0,0})-\lambda_{wn}\frac{1}{DZ(-1)}(w_{-1,0}+w_{0,0}\\
&\left.-w_{-1,-1}-w_{0,-1})\right]+\frac{\frac{1}{2}}{DZ(-1)+DZ(0)}\\
&\times\left[\mu_{se}\frac{1}{DX(0)}(w_{1,0}+w_{1,1}-w_{0,0}-w_{0,1})\right.\\
&+\mu_{sw}\frac{1}{DX(-1)}(w_{0,0}+w_{0,1}-w_{-1,0}-w_{-1,1})\\
&-\mu_{ne}\frac{1}{DX(0)}(w_{1,-1}+w_{1,0}-w_{0,-1}-w_{0,0})\\
&\left.-\mu_{nw}\frac{1}{DX(-1)}(w_{0,-1}+w_{0,0}-w_{-1,-1}-w_{-1,0})\right], \qquad \text{(A-3)}
\end{aligned}
$$

and

$$L_w(u,w) = 2\frac{1}{DX(-1)+DX(0)}\left(\mu_e\frac{w_{1,0}-w_{0,0}}{DX(0)} - \mu_w\frac{w_{0,0}-w_{-1,0}}{DX(-1)}\right) + 2\frac{1}{DZ(-1)+DZ(0)} \times \left((\lambda_s+2\mu_s)\frac{w_{0,1}-w_{0,0}}{DZ(0)} - (\lambda_n+2\mu_n)\frac{w_{0,0}-w_{0,-1}}{DZ(-1)}\right)$$
$$+ \frac{\frac{1}{2}}{DX(-1)+DX(0)}\left[\mu_{es}\frac{1}{DZ(0)}(u_{0,1}+u_{1,1}-u_{0,0}-u_{1,0}) + \mu_{en}\frac{1}{DZ(-1)}(u_{0,0}+u_{1,0}-u_{0,-1}-u_{1,-1}) - \mu_{ws}\frac{1}{DZ(0)}(u_{-1,1}+u_{0,1}-u_{-1,0}-u_{0,0}) - \mu_{wn}\frac{1}{DZ(-1)}(u_{-1,0}+u_{0,0}-u_{-1,-1}-u_{0,-1})\right]$$
$$+ \frac{\frac{1}{2}}{DZ(-1)+DZ(0)}\left[\lambda_{se}\frac{1}{DX(0)}(u_{1,0}+u_{1,1}-u_{0,0}-u_{0,1}) + \lambda_{sw}\frac{1}{DX(-1)}(u_{0,0}+u_{0,1}-u_{-1,0}-u_{-1,1}) - \lambda_{ne}\frac{1}{DX(0)}(u_{1,-1}+u_{1,0}-u_{0,-1}-u_{0,0}) - \lambda_{nw}\frac{1}{DX(-1)}(u_{0,-1}+u_{0,0}-u_{-1,-1}-u_{-1,0})\right]. \quad \text{(A-4)}$$